Determining erosion mechanisms in caves using 3D scanning

Max Cooper

August 20, 2019

1 Introduction

Caves are well known for their ability to preserve the past, including paleontological and archaeological remains. They also act as repository for dateable sediments that have been used to measure rates of landscape evolution [e.g. *Granger et al.*, 1997, 2001]. Further, as the cave passages morphology is due to incision into bedrock, they fit under the definition of a bedrock channel of *Turowski et al.* [2008]. Such channels are well known to record past conditions such as climate, tectonics, and hydrology in their geometry [e.g *Finnegan et al.*, 2005; *Stark*, 2006; *Wobus et al.*, 2006, 2008; *Amos and Burbank*, 2007; *Turowski et al.*, 2007, 2009; *Yanites and Tucker*, 2010]. Cave passages have an additional advantage over to surface bedrock channels as they are preserved from surface erosion, and have the ability to remain in a landscape over millions of years *Palmer* [2007b]; *Gabrovšek* [2002]; *Osborne* [2007]; *Broak* [2008]; *Plotnick et al.* [2015]. Further, some passages contain cuspate bedforms known as scallops, the geometry of which is known to be a function of local shear stress *Curl* [1966, 1974]; *Blumberg and Curl* [1974], providing a unique record indicative of past, formative flow conditions.

Despite the amazing potential of cave morphology as a record of the past, the erosive mechanisms that form caves in turbulent flow are not well constrained, such as the relative importance of mechanical erosion versus dissolution [*Covington et al.*, 2015]. In fact, the type of dissolution that forms caves in turbulent flow is also not fully understood. The rate at which limestone dissolves is controlled by a rate limiting step (i.e. the rate of the slowest process) that can be either the rate of conversion of the mineral phase to ions, termed surface reaction rate limited dissolution, or the rate at which the ions move through a boundary layer into the bulk fluid, termed transport limited dissolution. Numerical modeling of transport and surface dissolution using surface reaction rates determined experimentally by *Plummer et al.* [1978] suggest that only surface reaction rate limited dissolution occurs when limestone is being dissolved in turbulent flow [*Dreybrodt and Buhmann*, 1991; *Covington*, 2014]. If it is the case that only surface reaction rate limited dissolution occurs, forms that depend on transport rates such as scallops [*Curl*, 1966] should not form if the hypothesized mechanism of formation is correct [*Covington*, 2014]. While models suggest they should not form, scallops are abundant in many caves all over the world. As such, it is important to further constrain erosion mechanisms between surface reaction rate limited dissolution, transport limited dissolution, and mechanical erosion. These erosion mechanisms can also mix, such as the dissolution of gypsum exhibiting a mix of surface and transport rates.

This study aims to constrain erosion mechanisms in caves. One approach to determining mechanisms is to measure shear stress (τ_b) from scallops, and to measure erosion rate, as erosion can be modeled as a power law of shear stress with the exponent, a, related to mechanism [*Whipple et al.*, 2000]. The shear stress erosion model is

$$E = K\tau_b^a\,, \tag{1}$$

where K is a constant. *Whipple et al.* [2000] give likely values of a for different mechanical mechanisms such as plucking of jointed blocks ($1 \lesssim a \lesssim 3/2$) and abrasion by sediment ($a = 5/2$). While plucking of grains detached following boundaries loosened by dissolution has been observed in soluble rocks [*Levenson and Emmanuel*, 2016] and on other corroding materials [*Guo et al.*, 2006], it has not been narrowed to a specific value of a. Transport limited dissolution, where dissolution rate is proportional to the boundary layer thickness, scales with $a = 1/2$ [e.g. *Perne et al.*, 2014]. For surface reaction rate limited dissolution, as predicted on limestone for turbulent flow [*Dreybrodt and Buhmann*, 1991; *Liu and Dreybrodt*, 1997; *Covington*, 2014], $a = 0$ as this process depends solely on chemistry and not flow. Dissolution experiments on gypsum show $1/3 \leq a \leq 1/2$ [*Opdyke et al.*, 1987] due to mixed transport/reaction rate kinetics. Shear stress in this model can be found from scallop length as

$$Re^* = \frac{L\sqrt{\tau_b/\rho}}{\nu}, \tag{2}$$

where $Re^* = 2200$ is the scallop roughness Reynolds number, L is the length of of the scallop, ρ is the fluid density, and ν is the fluid kinematic viscosity, as determined by dimensional analysis and experiments in gypsum [*Curl*, 1974; *Blumberg and Curl*, 1974]. Methods to measure E include calculation from water chemistry [e.g. *Covington et al.*, 2015] and direct measurement with limestone tablets or micro-erosion meters [*Gabrovšek*, 2009]. However, both methods are problematic as calculation from chemistry relies on dissolution models, and the placement of limestone tablets or pins for micro-erosion measurements disrupt the flow structures required to form scallops in the direct measurement case.

However, meandering cave channels with scallops may provide a novel way of determining erosion mechanism as they preserve two pieces of information, the angle of incision, and a ratio of shear stress (Fig. 1). If the exponent in the erosion model is higher for instance, there is a greater rate of erosion in the direction of the wall for a single ratio of shear stress. Therefore, to understand shear stress distributions and relative incision rates in meandering soluble bedrock channels morphological data in the form of wall incision angles and scallop distributions are collected in several caves. To handle the large amount of scallops required to be measured these meanders are captured with low-cost 3D scanning methods, two of which are compared for their feasibility in capturing the large scale morphology of meandering

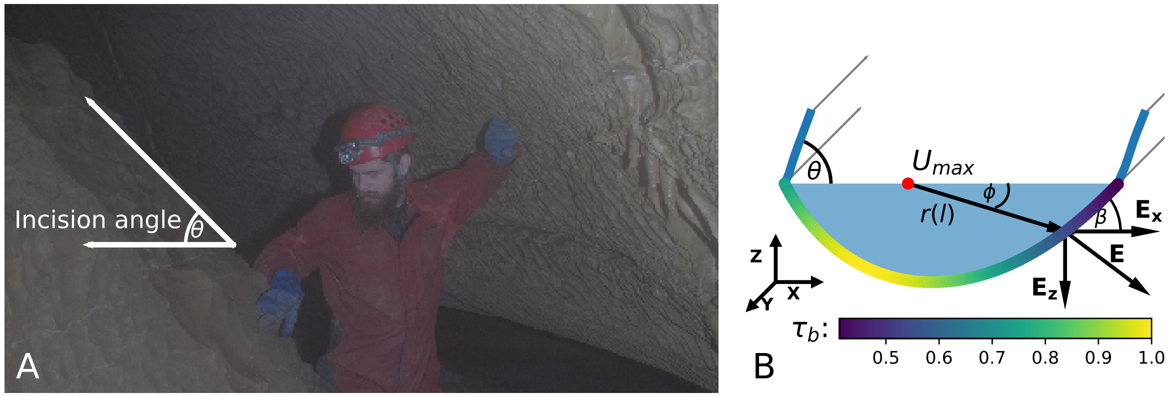

Figure 1: (A) A photograph in Copperhead Cave showing the incision angle around a meander bend. Scallop sizes on the outside of the bend are about half the size of those on the inside. (B) Schematic of the model. U_{max} is the position of the maximum velocity, offset from the center as a result of channel curvature in a meander. E, E_z, and E_x are the perpendicular, vertical, and horizontal erosion vectors, respectively. Colored floor indicates the current active channel, with color corresponding to τ_b normalized by its maximum value.

passages as well as the small scale morphology of scallops. These data are then compared to simulations of cross-section evolution within meander bends to interpret erosion mechanisms.

2 Cave Scanning

The 3D capture of cave morphology has increasingly been performed for over a decade as of 2019 with terrestrial laser scanning (TLS). This method uses a base station including a laser and a spinning mirror to acquire a cloud of points in a rotating arc around the station [*Mohammed Oludare and Pradhan*, 2016]. While TLS can produce very accurate reconstructions of morphology, the base station unit is historically bulky, making its use in smaller cave passages difficult. While increasingly smaller TLS devices are being built and used in 3D cave capture [*Kregar et al.*, 2019], they do remain expensive and typically cost more than $10,000. On the other hand, over the same span of time lower cost methods of capturing 3D models of the environment have been developed. These methods are Structure from Motion (SfM), commonly used in constructing 3D models from aerial photographs, in archaeology, and other general uses such as for video games and movies, and Simultaneous Localization and Mapping (SLAM), which is tailored for robotics applications such as self-driving vehicles [*Cadena et al.*, 2016].

Both methods of low-cost 3D scanning use easily available, cheap sensors. For SfM any camera can be used and regular photographs taken *James and Robson* [2012], while for SLAM the sensor can be a camera capturing video (monocular SLAM), a pair of cameras arranged for stereo video, or a novel sensor called an RGB-D sensor, which captures regular (RGB), and depth (D) images in a video stream [*Cadena et al.*, 2016]. These depth images are acquired by projecting a pattern of infrared light (termed *structured light*) that is deformed by an object, and captured with an infrared camera. The obtain depth information the SfM or monocular SLAM concept works similarly to a part of human vision; objects closer to the sensor move faster than objects in the background [*James and Robson*, 2012]. These objects are picked using an algorithm such as scale invariant feature transform (SIFT) that identifies unique points in an image and the points tracked between images [*Lowe*, 2004]. For SLAM using RGB-D the depth information is provided by the structured light sensor. These methods both require tracking between multiple photographs (SfM) or video frames (SLAM). In the SfM or monocular SLAM case tracking is performed as in the depth sensing portion, while SLAM using RGB-D can track either using the same method as SfM, or by matching curvature extracted from the depth image.

These two methods contrast in their goals for the reconstructed model. While they both seek to produce the best reconstruction possible, SLAM aims to produce a real-time reconstruction in a computationally inexpensive way, compared to SfM which is performed after-the-fact. These goals are reflected in the overall reconstruction algorithm, where SfM treats all images acquired, adjusting the identified points to minimize error over an entire reconstruction (bundle adjustment), similar to loop closure in a cave survey. For SLAM algorithms the real-time nature does not allow the treatment of the entire set of collected frames, but instead only tracks based on some number of previous frames and the model being built. State-of-the-art SLAM algorithms such as Kintinuous [*Whelan et al.*, 2015a] and ElasticFusion [*Whelan et al.*, 2015b] do however treat loop closures and adjust the model in a similar way to SfM, however with less points in the minimization to lower the amount of computation. A negative to not treating all images is drift, which these available state-of-the-art available algorithms try to handle. Even more current algorithms [e.g. *Puri et al.*, 2017; *Houseago et al.*, 2019] utilize inertial measurement units (IMUs), which track movement of the sensor to aid in reconstruction perform even better at reconstruction, however no software at the time of this report implement these algorithms is available.

The cave environment produces a unique challenge for both of these low-cost scanning methods, mainly due to low light. As SfM requires well lit photographs, and the lighting must be similar for point tracking to work, a good light source is needed with no focal spot. Additionally, longer exposure time or gain (ISO) is needed for decent quality images. Due to the lighting requirement, and the video acquisition nature of SLAM, tracking from RGB in the cave environment is even more difficult, as exposure times cannot be long when collecting 25-30 frames per second from the sensor. However, as non-visual SLAM algorithms can use the depth map for tracking, SLAM is a potential candidate for cave scanning. Despite this challenge, both methods have been used for scanning caves with success. For instance *Mankoff et al.* [2017] constructs large scale scans of sub-glacial conduit with SfM, and uses SLAM for smaller scale features. While they observed that SLAM failed for large scale, it is tested in this study for medium scale scanning for its applicability in meander bends.

3 Methods

3.1 Scanning

Both low cost methods were tested for their applicability for scanning in meander bends, Simultaneous Localization and Mapping (SLAM), and Structure from Motion (SfM). Data for SLAM were collected using an Orbbec Astra S RGB-D sensor. This sensor is mounted via 1/4” thread to a camcorder grip for stabilization, with lighting provided by a wide angle LED headlamp (ZebraLight) also mounted to the grip. For SLAM a logging computer is required. To minimize the size of the data collection setup an Intel Compute Stick was used for logging with a heads-up display (Vufine+ Wearable Display) used to view the RGB-D stream. The collected data was processed on a high-end workstation with a powerful GPU (NVIDIA Quadro K4000, 2.2TFLOPS) using the ElasticFusion algorithm, one of the current state-of-the-art SLAM algorithms. To obtain the best reconstructions in low light settings were chosen in ElasticFusion to weight the depth images 100% versus RGB images for tracking.

For SfM data is simply photographs collected via camera. Lighting for these images is provided by the wide angle LED headlamp either helmet mounted, or attached to the camera via the 1/4” thread. The software used for reconstruction for SfM was AgiSoft PhotoScan (now AgiSoft Metashape).

For either method the scans were referenced to a coordinate system orthogonal to gravity for wall angle measurements. The coordinate system information is generated from a cave survey with markers as stations placed as not to obscure scallops. Survey data were collected with a DistoX2 laser range finder, which measures length, azimuth, and inclination. For each station three shots were taken and the average values used as the data point. This instrument is accurate to 2 mm for distance at up to 10 meters, and 0.5° for angular measurements [*Trimmis*, 2018]. Survey data were logged to the cave survey software TopoDroid [https://github.com/marcocorvi/topodroid] then processed into x, y, z points in Cave3D [https://github.com/marcocorvi/cave3d]. To reference scans in AgiSoft PhotoScan virtual markers are placed where they appear on individual photographs and the coordinates of the markers entered into the referencing tool. For scans generated by ElasticFusion both the scan and the x, y, z points from Cave3D are loaded into a software package for analysing point clouds, CloudCompare [https://www.danielgm.net/cc/]. The scan is then rotated and translated roughly so the survey coordinates align with markers visible in the scan. After rough alignment the point pair picking Align tool is used with a point on the marker and the corresponding point in the survey are chosen as point pairs. For both scan types the survey additionally acts as a ground truth, and the accuracy of each method can be established.

3.2 Meander data processing

For the erosion mechanism determination portion of this study locations for scanning were picked by identifying places in the caves where the opposite walls in meander bends have roughly the same angle (less than 10 degree disparity). After reconstruction the individual walls were cropped using the Cross-Section tool in CloudCompare software. Planes were fit to the cropped walls with RANSAC Shape Detection tool [*Schnabel et al.*, 2007], which samples points repeatedly to find the best model and remove outliers [*Fischler and Bolles*, 1987]. The dip of the plane was recorded as the incision angle. Scallops were measured on each wall in PhotoScan. The recorded scallop size (L) was the longest distance parallel to flow as per *Curl* [1974]. To constrain parameters in the numerical model floor slope measurements were also taken by fitting a plane to the floor of caves in CloudCompare.

For scallops measurements *Curl* [1974]; *Blumberg and Curl* [1974] suggest using Sauter-mean,

$$L_S = \frac{\sum L_i^3}{\sum L_i^2}, \tag{3}$$

as a characteristic size within a scallop population, since the larger scallops are more indicative of wall shear stress. To measure contrasts in shear stress from scallops the ratio of sizes is needed, rather than the mean of all scallop lengths. As such Sauter-mean of the inner wall, L_I, and outer wall, L_O, were computed separately. The ratio computed is L_I/L_O as shear stress on the outer wall is greater than that on the inner. To estimate confidence limits on the observed ratios bootstrap Monte Carlo with replacement is used, where a random sample of scallop lengths is taken from either wall, and the ratio from that random sample is computed. This operation is then repeated with a different sample from the set. Approximately

50 scallops were randomly sampled from each wall 1000 times, and the Sauter-means were calculated for each random sample. Scallop ratio and incision angle measurements were fit to a linear model using orthogonal distance regression, as both the ratios and angles have associated uncertainty. To compare field data to modeled meanders, confidence bands on the measured data are plotted at the 95% level.

3.3 Numerical meander model

To model incision angles in meander cross-sections a shear stress estimation method termed the WTA method [*Wobus et al.*, 2006, 2008] was used and the cross-section is updated with erosion rate as a power law of shear stress, with the exponent reflective of erosion mechanism (Eq. 1). The WTA method uses the law of the wall to approximate τ_b around a channel perimeter given cross-section geometry, discharge (Q), slope (S), and roughness length (z_0). To approximate the asymmetry of bed stresses found within a meander bend, the position of maximum velocity is offset from the center of the free-surface to a position between the left wall of the channel and the center of the free-surface (Fig. 1). The general algorithm of the WTA method is:

1. Determine the water height, h, by minimizing the difference between prescribed Q and discharge computed by the Chézy equation with h dependent wetted area, A, and perimeter, P.

2. Calculate the maximum velocity, U_{max}, using the law of the wall over all rays, $r(l)$, from maximum velocity position to x, z points on the wall and requiring the average velocity within the cross-section to satisfy $u = Q/A$.

3. Solve the modified law of the wall equation for the bed-normal velocity gradient,

$$\left.\frac{du}{dr(l)}\right|_{z_0} = \frac{U_{max}}{z_0} ln(r(l)/z_0)^{-1} \cdot sin(\phi - \beta)\,. \tag{4}$$

Angles ϕ and β are illustrated in Fig. 1b.

4. Calculate τ_b for all points along the perimeter via

$$\tau_b(l) = \varphi\rho A\left(\frac{du}{dr(l)}\bigg|_{z_0}\right)^2. \tag{5}$$

The factor, φ, ensures force balance,

$$\varphi = \frac{gS}{\sum_{i=1}^{N}\left(\frac{du}{dr(l)}\big|_{z_0}\right)^2 dl(i)}, \tag{6}$$

where g is gravitational acceleration, and $l(i)$ is the distance between the i and $i-1$ x, z point defining the perimeter.

At each time step this algorithm was used to calculate τ_b for each point along the perimeter. The channel is then evolved per-point perpendicularly to the wall with the length a function of shear stress (Eq. 1). Simulations are run until the active channel width does not change over 100 time steps. Simulations were run with parameters Q, S, and z_0 that are representative of caves in this study. Roughness height, z_0, is the least constrained variable and is assumed to be on the order of 1cm [*Palmer*, 2007a]. Here $z_0 = D/30$ for hydraulically rough flow [*Nikuradse*, 1950]. For every simulation the equilibrium shear stress distribution along the channel, incision angle, and mean shear stress from the previous 100 time steps on the left and right wall are recorded along with the input parameters (a, Q, S, z_0). A value $a = 0.1$ is used to approximate surface reaction rate limited dissolution as simulations with $a = 0$ (the true reaction limited case) do not reach equilibrium [*Cooper and Covington*, in prep].

4 Field Sites

Several field sites are used in this study including caves in Tennessee, Arkansas, and New Mexico. Preliminary fieldwork to test scanning methods was conducted in Gourdneck Cave in Tennessee and Chilly Bowl Cave in Arkansas. As these were preliminary tests and not to collect data on meander bends geologic or other data such as floor slopes or sediment presence was not collected.

Data collection to determine erosive methods in the form of incision angles and scallop lengths on opposite walls was collected in two caves, Parks Ranch Cave (PRC) and Copperhead Cave (CHC). PRC is located in Eddy County, New Mexico, USA, formed within the Castile Formation, a gypsum unit [*Stafford et al.*, 2008]. Water enters PRC through several surface channels and sinkholes, and drains into Chosa Draw, a tributary of the Black River. The active stream channel contains water through the entire year and some sediment. Evidence of flooding to the ceiling is visible throughout PRC, even in passages at higher elevation. Slope values are $1/2 - 3°$. Measurements were recorded in a series of meander bends located in a tributary to the main stream near the most northwestern entrance.

CHC is located in Newton County, Arkansas, USA, and is formed in the St. Joe member of the Boone Formation. CHC contains water year round in one major stream passage that empties into a tributary of the Buffalo River [*Gillip*, 2007]. This passage is mainly meandering canyon, with some areas having remnant phreatic tubes near the ceiling. The stream contains chert gravel and larger clasts weathered from the Boone Fm, a unit with a high chert content. Measurements were recorded in a section of stream upstream of a knickpoint where slope is $1/2 - 1°$ and sediment is sparse. Downstream from the measured section there are higher slopes and larger clasts.

5 Results

5.1 Preliminary scanning

To test the quality of reconstructed scans from SfM and SLAM preliminary scans were taken in each cave listed above. The first preliminary scan was taken in Gourdneck Cave to test the accuracy of the SfM method with a coordinate system referenced to a survey. Images for reconstruction were taken with a mirrorless Sony A6000 camera with lighting provided by helmet mounted wide angle headlamp. Images were collected in a passage immediately downstream of a waterfall with survey markers placed throughout the scanned passage. This region of the cave contains a closed loop and as such is an excellent test of the ability for the SfM algorithm to reconstruct the geometry. Reconstruction in AgiSoft PhotoScan was successful, including the closed loop (Fig. 2), with a total distance error between the survey and the scan of 7 cm.

To test the accuracy of reconstruction from the SLAM algorithm ElasticFusion scans were taken in Chilly Bowl Cave. For comparison a reference survey and SfM scan were first taken in the "Boogie Tube" passage, a 30 m long phreatic tube (Fig. 3a). Images lit by helmet mounted headlamp were taken with the mirrorless camera. The total error between the survey and reconstructed scan is 18 cm over the entire passage Data for ElasticFusion were collected using the miniaturized scanning setup with an Orbbec Astra S RGB-D sensor. The scanning pattern for SLAM used was a sweep of the sensor oblique to the passage so that the floor, walls, and ceiling are all captured in one location while moving through the passage. Reconstruction of the entire passage was successful (Fig. 3b), however the reconstruction contains drift over the long scan. Additionally, although tracking was successful through most of the passage, a bend appears at the end of the passage in reconstruction which is not physically there and which does not appear in the SfM reconstruction.

While reconstruction from SLAM over a large distance was not accurate, its applicability for shorter scans in meander bends was tested in Copperhead Cave by comparison to a

Figure 2: (A) 3D model plan view of an area in Gourdneck Cave. (B) A view into the model towards the closed loop in the scan.

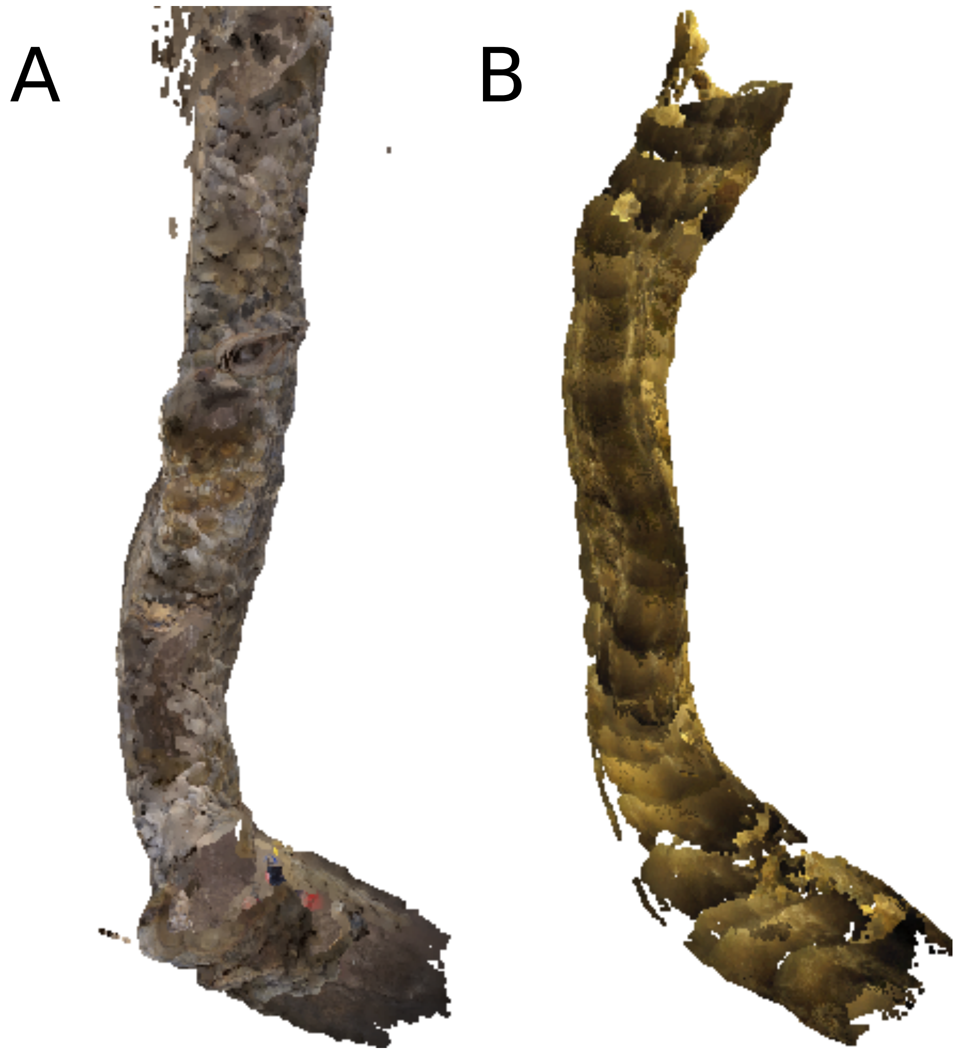

Figure 3: Two reconstructions of Boogie Tube in Chilly Bowl Cave, Arkansas. (A) Reconstruction from Structure from Motion in AgiSoft PhotoScan and (B) reconstruction from SLAM with ElasticFusion algorithm. SfM reconstruction produces a low error compared to survey, while SLAM reconstruction has drift over approximately 20 meters of passage.

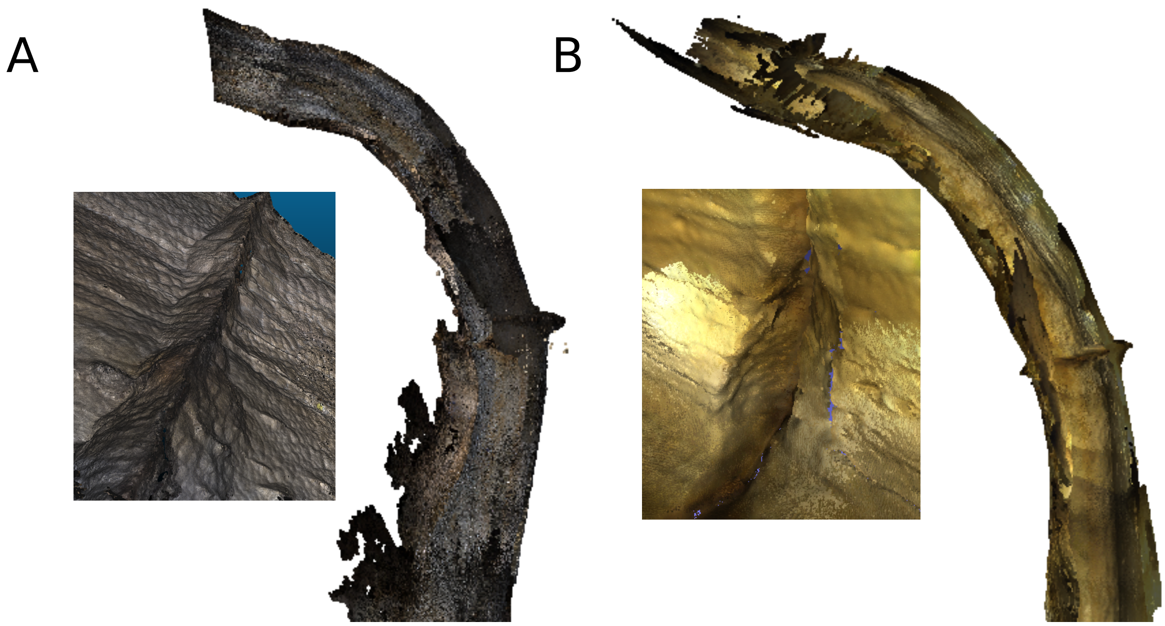

Figure 4: Reconstructions of the same meander bend in Copperhead Cave, Arkansas from (A) Structure from Motion and (B) ElasticFusion SLAM algorithm. Insets in A and B highlight the same region, with SfM reconstructing more detail of the scallops than SLAM.

reference survey and SfM reconstruction with an overall accuracy of 3 cm (Fig. 4a). Data for SLAM were collected in the same pattern as in Chilly Bowl Cave, however the sweeps here did not include the passage ceiling as the passage was tall and narrow. Reconstruction of the meander bend was successful with minimal drift (Fig. 4b) compared to the long scan in Chilly Bowl Cave, and no significant tracking errors occurred. However, despite the accurate reconstruction of the large scale passage morphology, the smaller scallops were not captured as well as in the SfM reconstruction (inset in Fig. 4b). Due to this limitation SfM was chosen as the scanning method for data collection in meander bends.

5.2 Meander data

Scallops and incision angles were measured from scans in seven locations in CHC, and eight locations in PRC. Data were also collected by hand at one location in PRC via caliper and inclinometer on a Brunton compass. Scans in CHC were taken with the Sony A6000 mirrorless camera, while those in PRC were taken with a Canon ELPH300 point-and-shoot

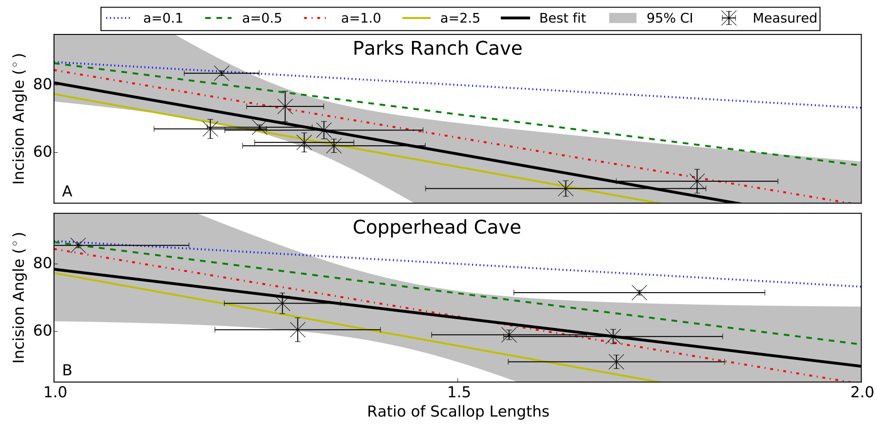

Figure 5: Channel incision angle versus the ratio of Sauter-mean scallop lengths on the inner and outer meander walls in Parks Ranch Cave (A) and Copperhead Cave (B). Data are fit using orthogonal distance linear regression as both incision angle and ratio have associated error values. Error bars for ratio of Sauter-means are the standard deviation, while they are the maximum and minimum values for incision angle. Colored lines are best fit lines to simulation runs with different values of the exponent, a, in the shear stress erosion model.

camera. All scans were referenced to surveys. The ratios of the Sauter-mean scallop lengths on either wall versus incision angle are plotted in Figure 5 for CHC and PRC, along with the 95% confidence band on the orthogonal regressions, and lines fit to the simulation results for different exponents, a, in the shear stress erosion model. Confidence intervals on ratios are the standard deviation as determined by bootstrap Monte Carlo, and confidence intervals on the incision angle are the maximum and minimum values. Simulation runs use the parameters $Q = 0.25$, $S = 0.035$, $z_0 = 0.0003$ and vary only the value of a. The choice of single values for these simulations is valid as varying these parameters do not statistically change the observed relationships, with only a affecting the slope of the relationship between scallop ratio and incision angle (Fig. 6).

For all cave sites there is a pattern of smaller scallops, and therefore higher shear stress, on the channel wall that is being undercut in the direction of migration. Similarly, there exists a general relationship of lower incision angles for larger contrasts in wall shear stress as erosion on the outer wall overwhelms that on the inner. The slope of this relationship differs between the two sites studied here, with PRC having a steeper negative slope than

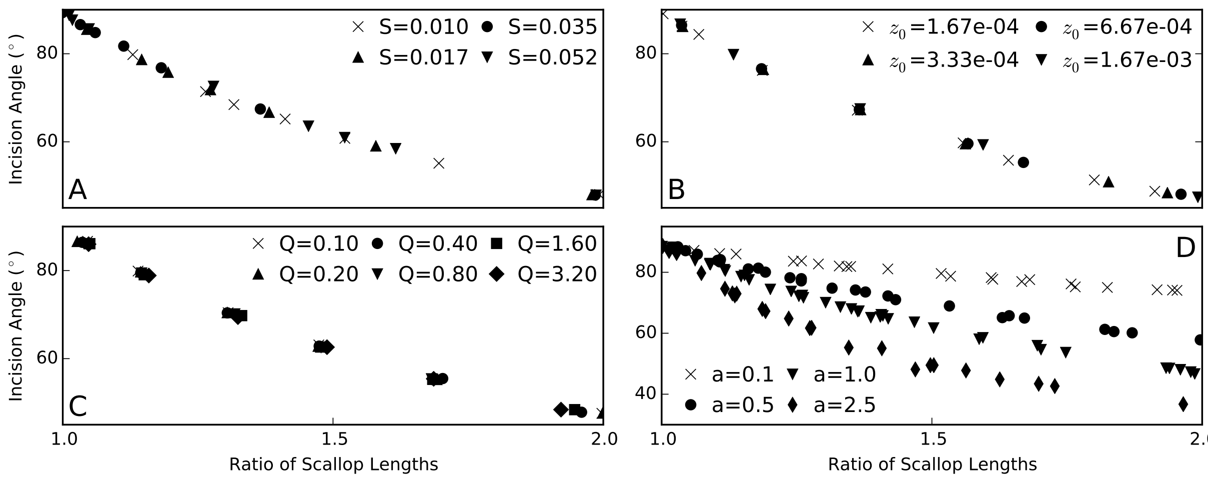

Figure 6: Influence of (A) slope, (B) roughness height, (C) discharge, and (D) erosion exponent on the relationship between scallop length ratio and channel incision angle. Within each panel the position of U_{max} was varied in order to produce a range of scallop lengths ratios and incision angles.

CHC, thus having a relationship closer to simulations where the power of shear stress was higher. For PRC $a = 0.1$ and $a = 0.5$ do not fit within the 95% confidence interval, while only $a = 0.1$ is not contained in the range for CHC. For Parks Ranch Cave the line of best fit for the data is nearly parallel to the relationship of $a = 1.0$, while Copperhead Cave data produce a best fit that is nearly parallel to the line for $a = 0.5$. The exponent $a = 1.0$ occurs for the mechanical process for plucking of jointed blocks, though neither PRC nor CHC contain the presence of plucked blocks.

6 Discussion

6.1 Low cost scanning methods for data collection

Both scanning methods used here are low cost, with each costing less than $1000 for data acquisition and lighting. The computational power for these is additionally more and more readily available, and can also be performed on cloud GPU platforms. Both methods used here are applicable to cave scanning, however they both have advantages and disadvantages.

For instance, while Structure from Motion provides excellent reconstructions both at the large (Fig. 3) and small scales (inset in Fig. 4a) in the same scan, data acquisition times are longer than Simultaneous Localization and Mapping (SLAM) sweeping, and reconstruction can take several hours to days for a large scan. However, the quality of data and low drift when to survey (e.g. 18 cm error over 30 m scan in the Boogie Tube passage) makes SfM superior for morphological measurements and the time required is worth investing. Additionally, if only a region of interest is captured with SfM the data acquisition and processing time can be lowered. In this study the region of interest can be made fairly small as each wall in the meander bend is treated independently.

On the other hand, SLAM has both fast acquisition and reconstruction. For short reaches SLAM produces decent reconstructions of large scale passage morphology (Fig. 4b), however it is prone to drift over large distances (Fig. 3b), even with the available state-of-the-art ElasticFusion algorithm. While it can capture the larger scale, smaller scale features such as scallops can be harder to pick out (inset in Fig. 4b) in these scans, and therefore it is not ideal for measuring such features when both large and small scale details are desired. Despite these drawbacks, SLAM is still a promising method if the goal is simply to capture the model, and if multiple short scans are taken they can be tied together with survey to capture large sections of a cave. Additionally, SLAM algorithms are continuing to be developed, and when tied with position sensors can produce superior results to ElasticFusion [e.g. *Puri et al.*, 2017; *Houseago et al.*, 2019], however, software incorporating these algorithms are not freely available. If such software is made available, and the algorithms improve, SLAM can become a powerful methods for generating 3D models, including for measuring morphology.

6.2 Erosion mechanisms in caves

The confidence bands on field data from Parks Ranch Cave and Copperhead Cave include several of the modeled lines for different values of a in the shear stress erosion model, indicating a range of possible values, and the exclusion of several. Both caves have bands that include $a = 1$ and $a = 2.5$, which are values for mechanical processes, with $a = 1$ representing plucking of jointed blocks, and $a = 2.5$ representing abrasion by sediment. CHC also contains $a = 0.5$, corresponding to transport limited dissolution. The best fit lines for each show PRC aligning with $a = 1$, and CHC with $a = 0.5$.

Confidence bands for either cave do not contain $a = 0.1$, representative of surface reaction rate dissolution. The presence of scallops, which require erosion to scale with boundary layer thickness/boundary shear stress, and the fact that the data are inconsistent with model runs with low values of a strongly suggest that the dominant type of erosion occurring in CH and PRC is not reaction rate limited dissolution; however, if combination of erosion processes are active, particularly if some of these are mechanical, this could explain the values obtained for a.

Inferring erosional mechanism from these data versus the models is not directly possible, as mixing produces intermediate values of a. For instance, combining transport limited dissolution with abrasion by sediment might produce $0.5 < a < 2.5$, which includes the values of a for plucking of jointed blocks, where $1 \leq a \leq 3/2$. Some processes, however, can be eliminated. While there is jointing present in both PRC and CHC, neither site shows physical evidence of plucked blocks following joints. Both caves contain sediment either sourced from outside of the cave (PRC), or possibly derived from weathering of material inside the cave (CHC). These sediments can become tools for abrasion during high discharges. Neither transport limited dissolution, nor reaction rate limited dissolution can be eliminated as a possible mechanism responsible for a portion of the erosion. The values $0.5 < a < 2.5$ suggest a mix of abrasion and some form of dissolution, whether transport limited, reaction rate limited, or mixed kinetics.

7 Conclusions

This study shows the ability to reconstruct 3D models of caves using two low-cost methods, Structure from Motion (SfM), and Simultaneous Localization and Mapping (SLAM). While both methods can produce reconstructions of the caves, SfM is the clear superior choice at this time as SLAM with the current available state-of-the-art algorithm, ElasticFusion, produces substantial drift at large scale, and while it provides an accurate reconstruction at the medium scale, small scale features are not included. SLAM still may be applicable for small scale scans of sediments or scallops. If multiple scans are tied together with survey, it may additionally scale upwards to the quality of SfM. SfM on the other hand, reconstructs both the large scale morphology accurately, for instance having less than 20 cm drift over 30 m in the Boogie Tube passage of Chilly Bowl Cave, and captures smaller scale features in large scale scans as in the meanders of Copperhead Cave.

By comparing data in the form of scallop ration and incision angles in meander bends, extracted from 3D scans, to modeled meander cross-sections, possible erosion mechanisms can be elucidated. The caves studied here, Parks Ranch Cave and Copperhead Cave both produce data that lie in the range of the simulated incision angle versus scallop ratio for various erosion mechanisms. Data from both caves eliminate surface reaction rate limited dissolution as the dominant mechanism for their formation, in contradiction with current speleogenesis theory which indicates that this type of erosion is the most important for caves with turbulent flow. While the data eliminates reaction rate limited dissolution as the sole cause of cave formation, it may be possible it does occur with a mix of processes such as abrasion from sediment. While the confidence bands and best fit lines to both sets of data constrain several types of erosion, it is important to not directly infer erosion processes from these data due to the mixing effect. To truly understand the erosional mechanisms each cave must be treated as a unique entity, with techniques such as those presented in this study, in combination with monitoring of erosion rates, water chemistry, and observations of sediment presence and other cave features.

8 Support and cave access

Funding for this study was in part from a grant from the Southesatern Cave Conservancy, Inc. (SCCI). Funding from this grant was used to purchase lights (ZebraLight wide angle headlamps), Orbbec Astra S (short range SLAM sensor) and Orbbec Astra (long range) RGB-D cameras, camcorder grips, and the logging computer for SLAM (Intel Compute Stick). Additionally, the grant was used for the purchase of an educational license of AgiSoft PhotoScan.

Access to Gourdneck Cave was granted by SCCI, and access to Copperhead Cave in the Buffalo National River area was granted by the National Park Service. Parks Ranch Cave is freely accessible as it is on Bureau of Land Management land. Chilly Bowl access was granted by private landowner.

References

Amos, C. B., and D. W. Burbank, Channel width response to differential uplift, *Journal of Geophysical Research: Earth Surface*, *112*(F2), 2007.

Blumberg, P., and R. L. Curl, Experimental and theoretical studies of dissolution roughness, *Journal of Fluid Mechanics*, *65*(4), 735–751, 1974.

Broak, P., Karst processes and time, *Geologos*, *14*, 19–36, 2008.

Cadena, C., L. Carlone, H. Carrillo, Y. Latif, D. Scaramuzza, J. Neira, I. Reid, and J. J. Leonard, Past, present, and future of simultaneous localization and mapping: Toward the robust-perception age, *IEEE Transactions on robotics*, *32*(6), 1309–1332, 2016.

Cooper, M. P., and M. D. Covington, Modeling cave cross-section evolution including sediment transport and paragenesis, *Earth Surface Processes and Landforms*, in prep.

Covington, M. D., Calcite dissolution under turbulent flow conditions: a remaining conundrum, *Acta Carsologica*, *43*(1), 195–202, 2014.

Covington, M. D., J. D. Gulley, and F. Gabrovšek, Natural variations in calcite dissolution rates in streams: Controls, implications, and open questions, *Geophysical Research Letters*, *42*(8), 2836–2843, 2015.

Curl, R. L., Scallops and flutes, *Transactions of the Cave Research Group of Great Britain*, *7*(2), 121–160, 1966.

Curl, R. L., Deducing flow velocity in cave conduits from scallops, *National Speleological Society Bulletin*, *36*(2), 1–5, 1974.

Dreybrodt, W., and D. Buhmann, A mass transfer model for dissolution and precipitation of calcite from solutions in turbulent motion, *Chemical Geology*, *90*(1), 107–122, 1991.

Finnegan, N. J., G. Roe, D. R. Montgomery, and B. Hallet, Controls on the channel width of rivers: Implications for modeling fluvial incision of bedrock, *Geology*, *33*(3), 229–232, 2005.

Fischler, M. A., and R. C. Bolles, Random sample consensus: a paradigm for model fitting with applications to image analysis and automated cartography, in *Readings in computer vision*, pp. 726–740, Elsevier, 1987.

Gabrovšek, F., *Evolution of karst: from prekarst to cessation*, Založba ZRC, 2002.

Gabrovšek, F., On concepts and methods for the estimation of dissolutional denudation rates in karst areas, *Geomorphology*, *106*, 9–14, 2009.

Gillip, J. A., The effects of land-use change on water quality and speleogenesis in ozark cave systems: A paired cave study of civil war and copperhead caves, northwestern arkansas, Ph.D. thesis, University of Arkansas, 2007.

Granger, D. E., J. W. Kirchner, and R. C. Finkel, Quaternary downcutting rate of the new river, virginia, measured from differential decay of cosmogenic 26al and 10be in cave-deposited alluvium, *Geology*, *25*, 107–110, 1997.

Granger, D. E., D. Fabel, and A. N. Palmer, Pliocene- pleistocene incision of the green river, kentucky, determined from radioactive decay of cosmogenic 26al and 10be in mammoth cave sediments, *Geological Society of America Bulletin*, *113*(7), 825–836, 2001.

Guo, H. X., B. T. Lu, and J. L. Luo, Non-faraday material loss in flowing corrosive solution, *Electrochimica acta*, *51*(25), 5341–5348, 2006.

Houseago, C., M. Bloesch, and S. Leutenegger, Ko-fusion: Dense visual slam with tightly-coupled kinematic and odometric tracking, in *2019 International Conference on Robotics and Automation (ICRA)*, pp. 4054–4060, IEEE, 2019.

James, M. R., and S. Robson, Straightforward reconstruction of 3d surface and topography with a camera: accuracy and geoscience applications, *Journal of Geophysical Research*, *117*(F03017), 2012.

Kregar, K., M. Vrabec, and D. Grigillo, Developing a robust workflow for acquisition of high-resolution full-3dcave topography, surface topography integration, and digital structuralmapping, in *EGU General Assembly Conference Abstracts*, vol. 21, 2019.

Levenson, Y., and S. Emmanuel, Quantifying micron-scale grain detachment during weathering experiments on limestone, *Geochimica et Cosmochimica Acta*, *173*, 86 – 96, doi: https://doi.org/10.1016/j.gca.2015.10.024, 2016.

Liu, Z., and W. Dreybrodt, Dissolution kinetics of calcium carbonate minerals in H2O-CO2 solutions in turbulent flow: the role of the diffusion boundary layer and the slow reaction H2O + CO2 -¿ H+ + HCO3-, *Geochimica Cosmochimica Acta*, *61*(14), 2879–2889, 1997.

Lowe, D. G., Distinctive image features from scale-invariant keypoints, *International journal of computer vision*, *60*(2), 91–110, 2004.

Mankoff, K. D., J. D. Gulley, S. M. Tulaczyk, M. D. Covington, X. Liu, Y. Chen, D. I. Benn, and P. S. Glowacki, Roughness of a subglacial conduit under hansbreen, svalbard, *Journal of Glaciology*, *63*(239), 423–435, 2017.

Mohammed Oludare, I., and B. Pradhan, A decade of modern cave surveying with terrestrial laser scanning: A review of sensors, method and application development, *International Journal of Speleology*, *45*(1), 8, 2016.

Nikuradse, J., *Laws of flow in rough pipes*, National Advisory Committee for Aeronautics Washington, 1950.

Opdyke, B. N., G. Gust, and J. R. Ledwell, Mass transfer from smooth alabaster surfaces in turbulent flows, *Geophysical Research Letters*, *14*(11), 1131–1134, doi:10.1029/GL014i011p01131, 1987.

Osborne, A. R. L., The world's oldest caves:-how-did they survive and what can they tell us?, *Acta carsologica*, *36*(1), 2007.

Palmer, A. N., *Cave Geology*, Cave Books, 2007a.

Palmer, A. N., Variation in rates of karst processes, *Acta Carsologica*, *36*, 2007b.

Perne, M., M. D. Covington, and F. Gabrovšek, Evolution of karst conduit networks in transition from pressurised flow to free surface flow, *Hydrology and Earth System Sciences Discussions*, *11*(6), 6519–6559, doi:10.5194/hessd-11-6519-2014, 2014.

Plotnick, R. E., F. Kenig, and A. C. Scott, Using the voids to fill the gaps: caves, time, and stratigraphy, *Geological Society, London, Special Publications*, *404*(1), 233–250, 2015.

Plummer, L. N., T. M. L. Wigley, and D. L. Parkhurst, The kinetics of calcite dissolution in CO2-water systems at 5 degrees to 60 degrees C and 0.0 to 1.0 atm CO2, *American Journal of Science*, *278*(2), 179, 1978.

Puri, P., D. Jia, and M. Kaess, Gravityfusion: Real-time dense mapping without pose graph using deformation and orientation, in *2017 IEEE/RSJ International Conference on Intelligent Robots and Systems (IROS)*, pp. 6506–6513, IEEE, 2017.

Schnabel, R., R. Wahl, and R. Klein, Efficient ransac for point-cloud shape detection, *Computer Graphics Forum*, *26*(2), 214–226, 2007.

Stafford, K. W., R. Nance, L. Rosales-Lagarde, and P. J. Boston, Epigene and hypogene karst manifestations of the castile formation: Eddy county, new mexico and culberson county, texas, usa, *International Journal of Speleology*, *37*, 83–98, 2008.

Stark, C. P., A self-regulating model of bedrock river channel geometry, *Geophysical Research Letters*, *33*(4), 2006.

Trimmis, K. P., Paperless mapping and cave archaeology: A review on the application of distox survey method in archaeological cave sites, *JOURNAL OF ARCHAEOLOGICAL SCIENCE-REPORTS*, *18*, 399–407, 2018.

Turowski, J. M., D. Lague, and N. Hovius, Cover effect in bedrock abrasion: A new derivation and its implications for the modeling of bedrock channel morphology, *Journal of Geophysical Research: Earth Surface*, *112*(F4), 2007.

Turowski, J. M., N. Hovius, A. Wilson, and M.-J. Horng, Hydraulic geometry, river sediment and the definition of bedrock channels, *Geomorphology*, *99*, 26–38, 2008.

Turowski, J. M., D. Lague, and N. Hovius, Response of bedrock channel width to tectonic forcing: Insights from a numerical model, theoretical considerations, and comparison with field data, *Journal of Geophysical Research: Earth Surface*, *114*(F3), 2009.

Whelan, T., M. Kaess, H. Johannsson, M. Fallon, J. J. Leonard, and J. McDonald, Real-time large-scale dense rgb-d slam with volumetric fusion, *The International Journal of Robotics Research*, *34*(4-5), 598–626, 2015a.

Whelan, T., S. Leutenegger, R. F. Salas-Moreno, B. Glocker, and A. J. Davison, Elasticfusion: Dense slam without a pose graph, in *Proceedings of Robotics: Science and Systems (RSS)*, 2015b.

Whipple, K. X., G. S. Hancock, and R. S. Anderson, River incision into bedrock: Mechanics and relative efficacy of plucking, abrasion, and cavitation, *Bulletin of the Geological Society of America*, *112*(3), 490–503, 2000.

Wobus, C. W., G. E. Tucker, and R. S. Anderson, Self-formed bedrock channels, *Geophysical Research Letters*, *33*(18), 2006.

Wobus, C. W., J. W. Kean, G. E. Tucker, and R. S. Anderson, Modeling the evolution of channel shape: Balancing computational efficiency with hydraulic fidelity, *Journal of Geophysical Research: Earth Surface (2003–2012)*, *113*(F2), 2008.

Yanites, B. J., and G. E. Tucker, Controls and limits on bedrock channel geometry, *Journal of Geophysical Research*, *115*(F04019), 1–17, 2010.